Letter

Measurement of additional radiation in the initial-state-radiation processes
$e^+e^- \to \mu^+\mu^-\gamma$ and $e^+e^- \to \pi^+\pi^-\gamma$ at BABAR

J. P. Lees, V. Poireau, V. Tisserand, E. Grauges, A. Palano, G. Eigen, D. N. Brown, Yu. G. Kolomensky,
M. Fritsch, H. Koch, R. Cheaib, C. Hearty, T. S. Mattison, J. A. McKenna, R. Y. So, V. E. Blinov,
A. R. Buzykaev, V. P. Druzhinin, E. A. Kozyrev, E. A. Kravchenko, S. I. Serednyakov, Yu. I. Skovpen,
E. P. Solodov, K. Yu. Todyshev, A. J. Lankford, B. Dey, J. W. Gary, O. Long, A. M. Eisner, W. S. Lockman,
W. Panduro Vazquez, D. S. Chao, C. H. Cheng, B. Echenard, K. T. Flood, D. G. Hitlin, Y. Li, D. X. Lin,
S. Middleton, T. S. Miyashita, P. Ongmongkolkul, J. Oyang, F. C. Porter, M. Röhrken, B. T. Meadows,
M. D. Sokoloff, J. G. Smith, S. R. Wagner, D. Bernard, M. Verderi, D. Bettoni, C. Bozzi, R. Calabrese,
G. Cibinetto, E. Fioravanti, I. Garzia, E. Luppi, V. Santoro, A. Calcaterra, R. de Sangro, G. Finocchiaro,
S. Martellotti, P. Patteri, I. M. Peruzzi, M. Piccolo, M. Rotondo, A. Zallo, S. Passaggio, C. Patrignani,
B. J. Shuve, H. M. Lacker, B. Bhuyan, U. Mallik, C. Chen, J. Cochran, S. Prell, A. V. Gritsan, N. Arnaud,
D. Bai, M. Davier, F. Le Diberder, L. Li, A. M. Lutz, G. Wormser, Z. Zhang, D. J. Lange, D. M. Wright,
J. P. Coleman, D. E. Hutchcroft, D. J. Payne, C. Touramanis, A. J. Bevan, F. Di Lodovico, G. Cowan,
Sw. Banerjee, D. N. Brown, C. L. Davis, A. G. Denig, W. Gradl, K. Griessinger, A. Hafner, K. R. Schubert,
R. J. Barlow, G. D. Lafferty, R. Cenci, A. Jawahery, D. A. Roberts, R. Cowan, S. H. Robertson,
R. M. Seddon, N. Neri, F. Palombo, L. Cremaldi, R. Godang, D. J. Summers,[*] G. De Nardo, C. Sciacca,
C. P. Jessop, J. M. LoSecco, K. Honscheid, A. Gaz, M. Margoni, G. Simi, F. Simonetto, R. Stroili, S. Akar,
E. Ben-Haim, M. Bomben, G. R. Bonneaud, G. Calderini, J. Chauveau, B. Malaescu, G. Marchiori,
J. Ocariz, M. Biasini, E. Manoni, A. Rossi, G. Batignani, S. Bettarini, M. Carpinelli, G. Casarosa,
M. Chrzaszcz, F. Forti, M. A. Giorgi, A. Lusiani, B. Oberhof, E. Paoloni, M. Rama, G. Rizzo, J. J. Walsh,
L. Zani, A. J. S. Smith, F. Anulli, R. Faccini, F. Ferrarotto, F. Ferroni, A. Pilloni, C. Bünger, S. Dittrich,
O. Grünberg, T. Leddig, C. Voß, R. Waldi, T. Adye, F. F. Wilson, S. Emery, G. Vasseur, D. Aston,
C. Cartaro, M. R. Convery, W. Dunwoodie, M. Ebert, R. C. Field, B. G. Fulsom, M. T. Graham, C. Hast,
P. Kim, S. Luitz, D. B. MacFarlane, D. R. Muller, H. Neal, B. N. Ratcliff, A. Roodman, M. K. Sullivan,
J. Va'vra, W. J. Wisniewski, M. V. Purohit, J. R. Wilson, S. J. Sekula, H. Ahmed, N. Tasneem,
M. Bellis, P. R. Burchat, E. M. T. Puccio, J. A. Ernst, R. Gorodeisky, N. Guttman, D. R. Peimer,
A. Soffer, S. M. Spanier, J. L. Ritchie, J. M. Izen, X. C. Lou, F. Bianchi, F. De Mori, A. Filippi, L. Lanceri,
L. Vitale, F. Martinez-Vidal, A. Oyanguren, J. Albert, A. Beaulieu, F. U. Bernlochner, G. J. King,
R. Kowalewski, T. Lueck, C. Miller, I. M. Nugent, J. M. Roney, R. J. Sobie, T. J. Gershon,
P. F. Harrison, T. E. Latham, and S. L. Wu

(BABAR Collaboration)

A dedicated measurement of additional radiation in $e^+e^- \to \mu^+\mu^-\gamma$ and $e^+e^- \to \pi^+\pi^-\gamma$ initial-state-radiation events is presented using the full BABAR data sample. For the first time results are presented at next-to- and next-to-next-to-leading order, with one and two additional photons, respectively, for radiation from the initial and final states. Comparison with predictions from PHOKHARA and AFKQED Monte Carlo generators is performed, revealing discrepancies in the one-photon rates and angular distributions for the former. This disagreement has a negligible effect on the BABAR measurement of the $e^+e^- \to \pi^+\pi^-(\gamma)$ cross section, but could affect other measurements significantly. This study sheds a new light on the longstanding discrepancy in this channel that affects the theoretical prediction of hadronic vacuum polarization contributions to the muon magnetic moment anomaly.

Introduction. The current Standard Model prediction [1] for the muon magnetic moment anomaly a_μ falls short of the direct measurement by 5.0σ [2,3], possibly indicating physics beyond the Standard Model. A leading source of uncertainty in a_μ arises from imprecise knowledge of the contribution of the hadronic vacuum polarization (HVP) evaluated from dispersion relations and measurements of the $e^+e^- \to$ hadrons cross section. The dominant channel in this cross section is $e^+e^- \to \pi^+\pi^-(\gamma)$, which furnishes 73% of the HVP contribution to a_μ. However, a long-standing discrepancy persists between the two most precise results using the initial-state radiation (ISR) technique, from *BABAR* [4,5] and KLOE [6–9]. The result from KLOE lies 2.9σ below that of *BABAR* in the region of the ρ resonance. Recent results from the CMD-3 experiment [10] with the energy scan technique lie above both *BABAR* and KLOE, exceeding them by 2.2σ and 5.1σ, respectively. This situation prevents a meaningful update of the a_μ prediction to compare with the new Fermilab measurement [3]. Tension is also observed with the lattice QCD evaluation [11–16] of the HVP contribution. The need to clarify these tensions and improve the precision on a_μ calls for further studies of the different approaches.

In this Letter we focus on higher-order radiative processes, likely to affect differently the various ISR experiments, namely the next-to-leading order (NLO) processes $e^+e^- \to \mu^+\mu^-\gamma\gamma$ and $\pi^+\pi^-\gamma\gamma$, and the next-to-next-to-leading order (NNLO) processes $e^+e^- \to \mu^+\mu^-\gamma\gamma\gamma$ and $\pi^+\pi^-\gamma\gamma\gamma$. Each photon can be emitted from the initial-state e^+ or e^-, or a final-state muon or pion (FSR). Building on our previous work [4,5], where very loose kinematical constraints were applied in order to reduce dependence on simulation, we make improved measurements of the relative contributions of events with two photons and study their kinematics. We then perform the first study of events with three photons.

Dataset and simulated samples. The analysis is based on 424.2 fb^{-1} (43.9 fb^{-1}) of data [17] collected at the SLAC PEP-II asymmetric e^+e^- collider operated at (and 40 MeV below) the $\Upsilon(4S)$ resonance. The *BABAR* detector and performance are described in detail elsewhere [18,19], and its response, including the variations of beam and detector conditions over time, is simulated with GEANT4 [20].

The two Monte Carlo (MC) generators used in this analysis are described in Appendix A. Signal processes $e^+e^- \to X\gamma(\gamma)$, with $X = \mu\mu$ or $\pi\pi$, are simulated with PHOKHARA with ten times the data statistics. Small samples of these processes are also simulated with the AFKQED generator. In both cases, one high-energy photon is generated within the detector angular range. PHOKHARA generation is limited to NLO, with up to one additional ISR or FSR photon emitted with an angular distribution according to the full NLO matrix element. AFKQED
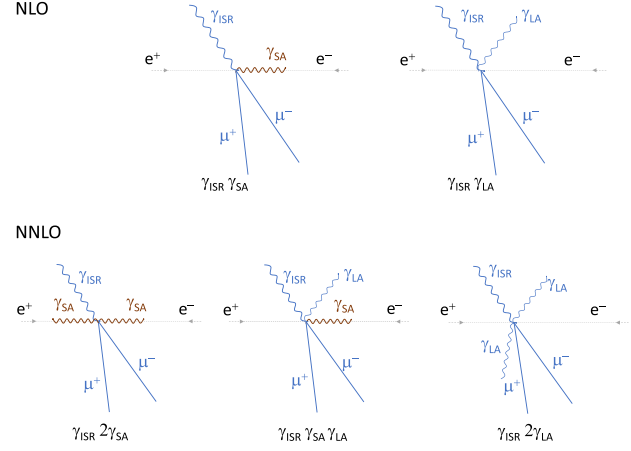

FIG. 1. Sketch of measured topologies for the ISR $\mu\mu\gamma$ (or $\pi\pi\gamma$) process at NLO and NNLO levels. Tracks and photons in blue are measured in the detector, undetected photons in red are assumed to be aligned with a beam.

provides NLO and NNLO simulated samples, within the approximation that the additional ISR photons are generated collinear to the beams.

Background ISR processes $e^+e^- \to K^+K^-\gamma(\gamma)$ and $e^+e^- \to X\gamma$ ($X = \pi^+\pi^-\pi^0, \pi^+\pi^-2\pi^0, \ldots$) are simulated with PHOKHARA and AFKQED, respectively. Background processes $e^+e^- \to q\bar{q}$ ($q = u, d, s, c$) are generated with JETSET [21] and $e^+e^- \to \tau^+\tau^-$ with KK2f [22]. As the models used in the generators for the background processes may be unreliable at low multiplicity or do not reproduce the measured hadronic spectra, data-driven corrections are applied to the MC estimations (Appendix B). Backgrounds mostly affect the pion channel while they are very low in the muon channel, mainly from well simulated $\tau\tau$ events.

Event selection. Radiative events are selected by requiring a detected photon in the laboratory polar-angle range $0.35 < \theta < 2.4$ rad, and with a measured energy $E_\gamma^* > 4$ GeV in the center-of-mass (c.m.) frame. Exactly two tracks of opposite charges are required to extrapolate to the collision region, each with: transverse momentum > 0.1 GeV/c, θ in the range 0.4–2.45 rad, at least 15 hits in the drift chamber. Events can contain any number of additional photons and tracks that do not satisfy the requirements. Detected photons with $E_\gamma > 50$ MeV and polar angle in the range 0.35–2.4 rad are retained for the fits described below. The photon with the highest measured energy in the c.m. frame is denoted γ_{ISR}. Events in which both tracks are tightly identified [19] as muons (pions) are assigned to the dimuon (dipion) sample. In the following, the rate of each radiative process is quoted as a fraction of the total yield in those dimuon and dipion samples, respectively. Topologies considered in the analysis are sketched in Fig. 1.

NLO study. The dimuon and dipion samples are submitted to two types of kinematic fits to $e^+e^- \to \pi^+\pi^-\gamma_{ISR}\gamma$, with one photon in addition to γ_{ISR}:

(i) $\gamma_{ISR}\gamma_{LA}$ fits: a photon γ_{LA} is detected at large angle (LA) to the beam, and its measured energy and angles are used in a fit.

(ii) $\gamma_{ISR}\gamma_{SA}$ fits: an undetected small angle (SA) photon γ_{SA} is approximated as being collinear with either beam.

Both NLO fits use the measured γ_{ISR} energy and direction, and the parameters and covariance matrices of the two tracks. To be consistent with the cross section measurement, the pion mass is assumed for both tracks [4,5]. All events undergo the $\gamma_{ISR}\gamma_{SA}$ fits while only events with at least one additional detected photon with $E_\gamma > 50$ MeV undergo the $\gamma_{ISR}\gamma_{LA}$ fits, taking each photon in turn. The fit with the lowest χ^2 is retained. An optimized contour in the $(\chi^2_{\gamma_{ISR}\gamma_{SA}}, \chi^2_{\gamma_{ISR}\gamma_{LA}})$ plane (so-called 2D-χ^2 selection) is used to reduce backgrounds. This only selection applied to the NLO samples retains 99% of the signal events, as determined in MC estimations and measured on the muon sample. Events are assigned to the NLO SA or LA samples according to the lowest χ^2 and if the additional photon energy exceeds 0.2 GeV. As γ_{LA} photons are measured in the detector, the energy threshold is expressed in the laboratory system, while for γ_{SA} ISR photons, it is set in the c.m. frame. Events that satisfy the 2D-χ^2, but not the energy, requirements are categorized as leading order (LO) events. We retain dimuons in the $m_{\pi\pi}$ mass range from threshold to 1.4 GeV/c^2 and dipions in the range between 0.6 and 0.9 GeV/c^2 around the ρ resonance where backgrounds are manageable (5.5% and 23% for the SA and LA pion samples, respectively, dominated by muon misidentification). For the dipion sample, the background from fake photons due to pion interactions in the calorimeter is measured in data and MC simulations and the relative excess of $(21.5 \pm 3.5)\%$ in data is corrected for.

In the SA samples, the energy distributions $E^*_{\gamma_{SA}}$ of the additional photon are shown in Fig. 2 for muons and pions. As expected from their ISR nature, the results of the two processes are consistent. A marked discrepancy between data and the NLO PHOKHARA predictions is observed, both in shape and normalization, in the dominant low-energy region.

This discrepancy is further investigated. The collinearity approximation of the γ_{SA} photon with the beams in the $\gamma_{ISR}\gamma_{SA}$ fit is found to induce energy- and polar-angle-dependent biases for both the χ^2 value and the γ_{SA} fitted energy, as determined in MC studies. However a comparison of the outputs of the $\gamma_{ISR}\gamma_{SA}$ and $\gamma_{ISR}\gamma_{LA}$ fits for events with a detected photon verifies with data that the $E^*_{\gamma_{SA}}$ bias is correctly simulated, hence is not responsible for the observed data to PHOKHARA discrepancy. A further test, independent from the NLO fits, is provided by a
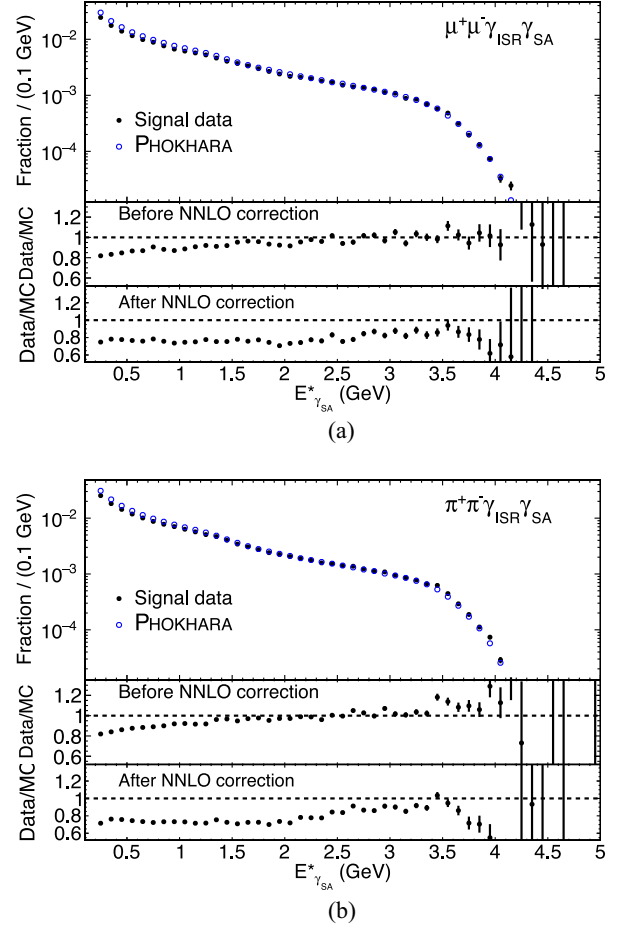

FIG. 2. Distributions of the fitted energy of the SA photon in the c.m. frame for the muon (a) and pion (b) samples. The data (full dots) are compared with PHOKHARA (open/blue dots) in each upper plot, and their ratio is shown in the middle plot. The lower plots show the ratio after the NNLO corrections discussed later in the text.

zero-constraint (0C) calculation of the energy and angles of the additional photon. With the constraint of 4-momentum conservation in $e^+e^- \to \pi^+\pi^-\gamma_{ISR}\gamma_{0C}$, the calculation uses the two track momenta and the γ_{ISR} direction. To avoid spurious γ_{0C} photons arising from shower fluctuations, the γ_{ISR} energy measurement is ignored and γ_{0C} candidates within a cone of 0.5 rad around the γ_{ISR} direction are excluded. The distributions of the polar angle $\theta_{\gamma_{0C}}$ for events with a calculated photon energy $E^*_{\gamma_{0C}}$ above 0.2 GeV, are shown in Fig. 3(a) for the data and PHOKHARA dimuon samples. Comparison reveals that PHOKHARA severely overestimates the NLO rate at small angles to the beams, with improving agreement at larger angles. As detailed studies demonstrate (Appendix C), this feature is not due to $\theta_{\gamma_{0C}}$ resolution. The data/ PHOKHARA ratio of the photon energy spectra $E^*_{\gamma_{0C}}$, shown in Fig. 3(b), reveals a mismatch between the LO and NLO rates and presents a positive slope, as in the $\gamma_{ISR}\gamma_{SA}$ fit.
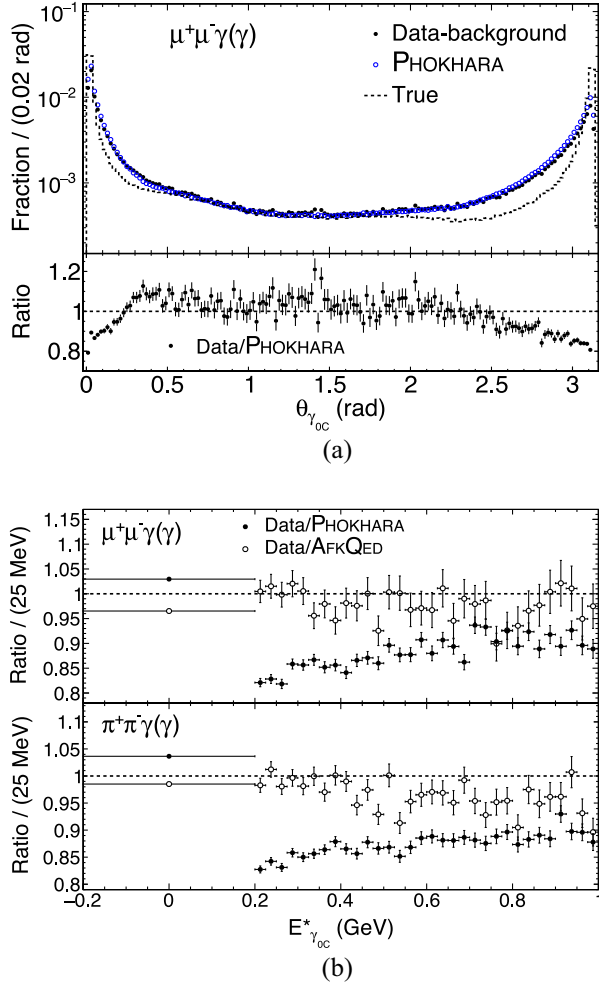
FIG. 3. (a) Distributions of the calculated polar angle $\theta_{\gamma_{0C}}$ for dimuon events with $E^*_{\gamma_{0C}} > 0.2$ GeV in the data (full dots) and PHOKHARA (open dots), along with the calculated $\theta_{\gamma_{0C}}$ using MC truth information (dashed histogram). (b) Ratios of data to PHOKHARA (full dots) and data to AFKQED (open dots) distributions of $E^*_{\gamma_{0C}}$ in the energy range below and above 0.2 GeV corresponding to LO and NLO, respectively, in muon (upper) and pion (lower) samples.

Since no angular assumption enters the 0C calculation, the observed energy dependence of the data/PHOKHARA ratio is thus not an artifact caused by the collinearity approximation of the γ_{SA} photon. In contrast to PHOKHARA, neither mismatch between the LO and NLO categories nor a data/MC energy slope are observed when conducting the same exercise with AFKQED.

In the LA samples, no energy dependence is observed in the data/MC ratio of the $E_{\gamma_{LA}}$ distributions from the $\gamma_{ISR}\gamma_{LA}$ fit, neither with PHOKHARA nor AFKQED, and the data to PHOKHARA discrepancy in normalization is much reduced. The relative contributions of ISR and FSR processes are measured using the minimum of the two angles in the laboratory frame between a track and the LA photon $\theta_{\min(trk,\gamma_{LA})}$ [5]. We observe clear peaks in the data and

MC distributions of this angle below 20°, due to FSR, over a broad distribution from LA ISR (Appendix D).

NNLO study. We then perform an NNLO analysis using three kinematic fits, $\gamma_{ISR}2\gamma_{SA}$, $\gamma_{ISR}\gamma_{SA}\gamma_{LA}$, and $\gamma_{ISR}2\gamma_{LA}$, where two photons are allowed in addition to γ_{ISR}. The SA photons γ_{SA} are approximated to be collinear with one of the beams and the LA photons γ_{LA} are measured in the detector. All events undergo the $\gamma_{ISR}2\gamma_{SA}$ fit, with one SA photon along each beam. Only events with at least one or two additional detected photons with $E_\gamma > 50$ MeV enter the $\gamma_{ISR}\gamma_{SA}\gamma_{LA}$ and $\gamma_{ISR}2\gamma_{LA}$ fits, respectively. No 2D-χ^2 selection is applied, and events are assigned to the $\gamma_{ISR}2\gamma_{SA}$, $\gamma_{ISR}\gamma_{SA}\gamma_{LA}$, or $\gamma_{ISR}2\gamma_{LA}$ sample if the χ^2 of that fit is lower than all others, including the NLO fits.

In all NNLO categories, the background from NLO events with spurious additional photons is estimated with the PHOKHARA sample, after correcting for data and MC rate differences observed above at LO and NLO levels. The non-NLO background is very small in the dimuon samples, but the dipion samples are affected by larger background from multihadronic ISR processes, especially those containing a π^0. This background is reduced by BDT (boosted decision tree) selections designed for each NNLO category (Appendix E). To further reduce background contributions, the fitted additional photons are required to pass energy thresholds specific to each NNLO category. After these selections, the NLO contribution to the background is dominant in all NNLO muon categories and pion $\gamma_{ISR}2\gamma_{SA}$. In the pion $\gamma_{ISR}\gamma_{SA}\gamma_{LA}$ and $\gamma_{ISR}2\gamma_{LA}$ samples, the multi-hadronic ISR contributions dominate but do not exceed 45% of the data. The NNLO data signal yields are obtained by subtracting both the NLO contribution and the estimated non-NLO background.

Significant NNLO signals are found in data in all $\gamma_{ISR}2\gamma_{SA}$, $\gamma_{ISR}\gamma_{SA}\gamma_{LA}$, and $\gamma_{ISR}2\gamma_{LA}$ categories. Results for the most abundant $\gamma_{ISR}2\gamma_{SA}$ category are summarized in Fig. 4, requiring $E^*_{\gamma_{SA}} > 0.2$ GeV for the most energetic SA photon and $E^*_{\gamma_{SA}} > 0.1$ GeV for the other. The χ^2 distributions and energy spectra of the SA photons are shown for muons (a), (c) and pions (b), (d). In both samples, the NLO background (solid/red histogram) dominates over the very low non-NLO background (dashed/blue histogram). The energy spectra of the SA photons for $\gamma_{ISR}2\gamma_{SA}$ signals in data are further compared to AFKQED predictions, where the AFKQED NNLO signals are restricted to the events with two SA photons that satisfy the energy thresholds.

Final results combining NLO and NNLO studies. Final results are obtained considering all NLO and NNLO radiative processes using a feedthrough probability matrix between true and reconstructed categories established with the PHOKHARA and AFKQED samples. Feedthrough contributions are estimated through an iterative procedure to
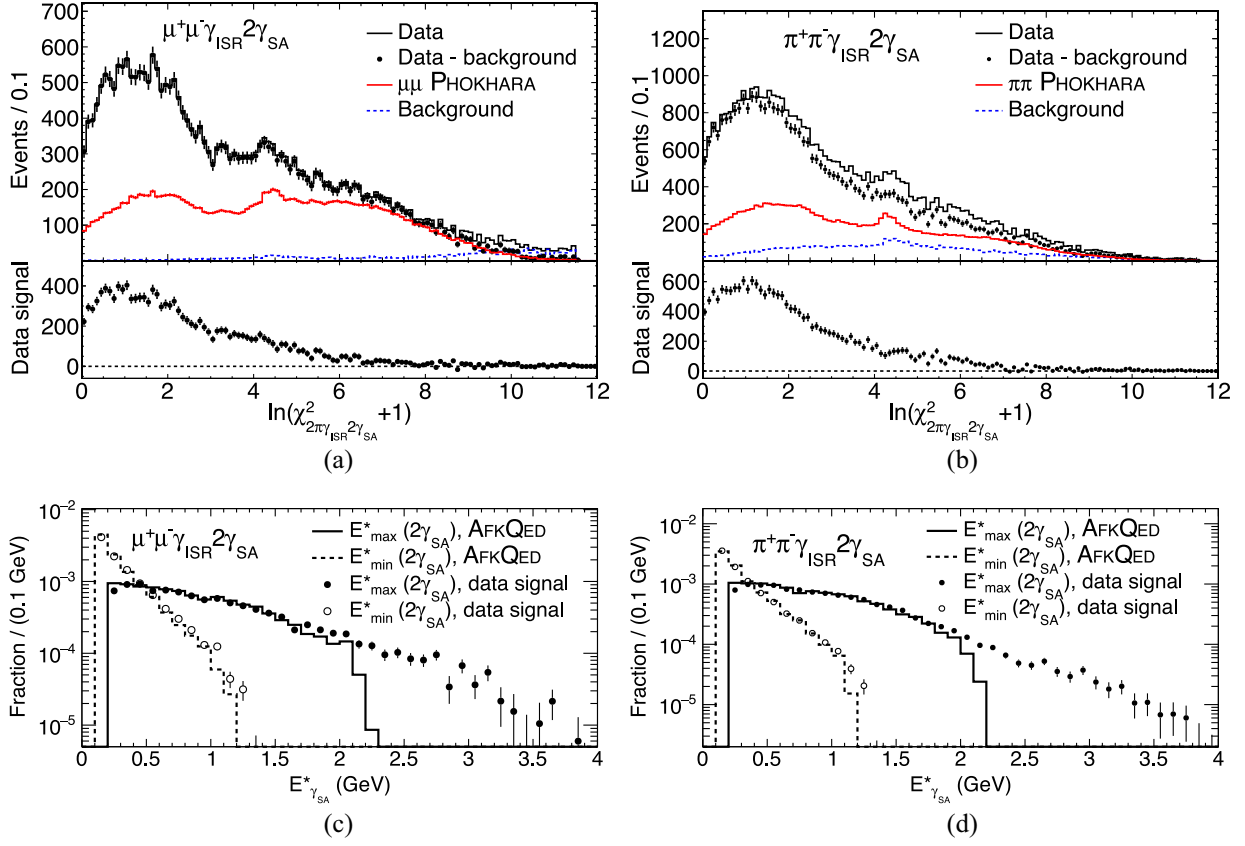
FIG. 4. Distributions of the χ^2 (a), (b) of the $\gamma_{\text{ISR}}2\gamma_{\text{SA}}$ kinematic fit for the muon (left) and pion (right) samples. The corresponding distributions (c), (d) of the c.m. energies of the more (full dots) and less energetic (open dots) SA photons after subtraction of backgrounds and NLO feedthrough, compared with AFKQED predictions (histograms), normalized to the data for $E^*_{\gamma_{\text{SA}}} < 2.3$ GeV.

correct for rate differences of each category in data and MC samples. Feedthrough yields estimated with AFKQED are corrected to account for its missing LA-ISR component.

The NLO $\gamma_{\text{ISR}}\gamma_{\text{SA}}$ rates and $E^*_{\gamma_{\text{SA}}}$ energy distributions are further corrected for a hidden NNLO feedthrough of the same size as the open $\gamma_{\text{ISR}}2\gamma_{\text{SA}}$ rate, due to the additional collinear ISR radiation: while double SA radiation from opposite beams is identified by the $\gamma_{\text{ISR}}2\gamma_{\text{SA}}$ fit, double SA radiation from the same beam cannot be distinguished from a single-photon radiation where the equivalent single photon merges the two γ_{SA} energies. The same-beam NNLO component in the measured $\gamma_{\text{ISR}}\gamma_{\text{SA}}$ spectrum is thus inferred from the sum of γ_{SA} energies in data $\gamma_{\text{ISR}}2\gamma_{\text{SA}}$ events, and subtracted. As shown in the bottom panels in Fig. 2, the NLO SA photon energy spectrum in data after the NNLO correction agrees better in shape with the PHOKHARA prediction, but it has a deficit in rate by more than 20%.

The final fractions of all fit categories with respect to the total event sample are given in Table I. The systematic uncertainties include those from efficiency corrections, background subtraction and feedthrough corrections with the latter two being the dominant contributions. Template fits to the $\theta_{\min(\text{trk},\gamma_{\text{LA}})}$ distributions in the $\gamma_{\text{ISR}}\gamma_{\text{LA}}$,

TABLE I. Event fractions in data for the $\mu\mu$ and $\pi\pi$ processes in all fit categories. The numbers in parentheses represent uncertainties, where the first is statistical and the second systematic. The results, except for NNLO 2LA (which is not simulated by any generator currently available), are corrected using efficiencies that vary category by category between 99% and 72%, except for NLO FSR $\pi\pi$ (40%) and NNLO FSR $\pi\pi$ (22% due to BDT selection).

Category	$\mu\mu$ $m_{\pi\pi} < 1.4$ GeV/c^2	$\pi\pi$ $0.6 < m_{\pi\pi} < 0.9$ GeV/c^2
LO	0.7716(4)(14)	0.7839(5)(12)
NLO SA-ISR	0.1469(3)(36)	0.1401(2)(16)
NLO LA-ISR	0.0340(2)(9)	0.0338(2)(9)
NLO ISR	0.1809(4)(35)	0.1739(3)(20)
NLO FSR	0.0137(2)(7)	0.0100(1)(16)
NNLO ISR[a]	0.0309(2)(38)	0.0310(2)(39)
NNLO FSR[b]	0.00275(6)(9)	0.00194(12)(50)
NNLO 2LA[c]	0.00103(3)(1)	0.00066(4)(4)

[a]NNLO ISR = 2SA-ISR or SA-ISR + LA-ISR.
[b]NNLO FSR = SA-ISR + LA-FSR.
[c]NNLO 2LA = 2LA-ISR, LA-ISR + LA-FSR or 2LA-FSR.

$\gamma_{\mathrm{ISR}}\gamma_{\mathrm{SA}}\gamma_{\mathrm{LA}}$, and $\gamma_{\mathrm{ISR}}2\gamma_{\mathrm{LA}}$ samples are used to estimate the fractions of FSR and large-angle ISR at the NLO and NNLO levels (Appendix D).

The results are summarized below:

(1) NNLO contributions are clearly observed with a total fraction of $(3.47 \pm 0.38)\%$ for muons and $(3.36 \pm 0.39)\%$ for pions. This allows the correction of NLO rates for cross feeds from NNLO categories. The corrected shape of the energy distribution for single SA photons provides further evidence, and good internal consistency.

(2) The NLO SA-ISR fractions in the PHOKHARA generator are higher than in the data, with data/MC ratios of 0.763 ± 0.019 for dimuons and 0.750 ± 0.008 for dipions, while the respective LA-ISR ratios, 0.96 ± 0.03 and 0.98 ± 0.03, are consistent with unity. This indicates a problem in the angular distribution of the NLO photon generated by PHOKHARA, with a large excess at small angles to the beams.

(3) The AFKQED generator provides a reasonable description of the rates and energy distributions of NLO and NNLO data. The sum of SA-ISR and LA-ISR rates in data up to the cutoff at 2.3 GeV photon energy applied at generation (Appendix A) leads to slightly high data/MC ratios of 1.061 ± 0.015 for muons and 1.043 ± 0.010 for pions.

(4) The ratio between data and the PHOKHARA prediction for NLO FSR is found to be 0.86 ± 0.05 for muons and 0.76 ± 0.12 for pions. The corresponding data/AFKQED ratios are 1.09 ± 0.06 for muons and 1.08 ± 0.10 for pions. In both cases, the ratio pion/muon is consistent with unity and supports the pion pointlike behavior for additional FSR. This result, obtained with a fake-photon subtraction that both includes a data/MC correction and takes into account NNLO feedthrough, supersedes the previous result of an excess of $(21 \pm 5)\%$ reported in the *BABAR* publication [4,5].

Consequences for the $\pi^+\pi^-(\gamma)$ cross section ISR measurements. The consequences of these findings for the $\mu^+\mu^-(\gamma)$ and $\pi^+\pi^-(\gamma)$ cross section measurements depend strongly on the experimental approach.

The *BABAR* measurements [4,5] are performed with a very loose selection that incorporates all NLO and higher order radiative processes. Therefore, no dependence on a particular event generator is introduced when handling additional radiation (Appendix F). Only the acceptance, determined using PHOKHARA, is affected by the generator shortcomings. However the acceptance correction of $(0.3 \pm 0.1) \times 10^{-3}$ is negligible compared to the estimated systematic uncertainty of 0.5% in the $\pi^+\pi^-(\gamma)$ cross section measurement [4,5].

In contrast, other experiments using the ISR approach [6–8,23,24] do not measure additional radiation.

While the total NLO correction in the cross section is strongly reduced by the near cancellation of the hard NLO terms by the infrared-finite sum of soft and virtual terms [25], each component is large and systematic uncertainties related to the undetected hard NLO contribution far exceed the theoretical uncertainty in the total NLO correction. The results of the present analysis question the validity of the procedure relying on PHOKHARA on two grounds: first, the hard NLO yield in PHOKHARA is significantly larger than our measurement, and second, NNLO contributions, absent in PHOKHARA, are found to be at a level larger than the systematic uncertainties quoted in Refs. [6–8,23,24]. A quantitative evaluation of these effects requires detailed studies of the specific experimental conditions, which is beyond the scope of this Letter. However the unique measurements reported here, and their implication for ISR experiments that rely on the PHOKHARA generator to account for unmeasured radiative events, offer new key insights that may allow progress in the longstanding quandary that affects the theoretical prediction of HVP contributions to a_μ, with respect to both the final value and its currently degraded precision.

Appendix A: Signal Monte Carlo generators. In this analysis, initial-state-radiation events $e^+e^- \to X\gamma$ are produced by Monte Carlo generators with a high-energy photon emitted at large angle to the beams. In PHOKHARA9.1 [26] complete NLO corrections to $e^+e^- \to \mu^+\mu^-\gamma$ and $e^+e^- \to \pi^+\pi^-\gamma$ are implemented. All NLO diagrams for virtual and real photon production are included, whether radiation occurs in initial or final state. For muons, matrix elements are given by QED for ISR, FSR, and interference. For pions, ISR radiation is given by QED while FSR is described by a pointlike model of the pion. No NNLO diagram is included. Up to one additional ISR or FSR photon is generated with an

angular distribution according to the full NLO matrix element.

The AFKQED generator is based on the formalism of Refs. [27,28]. Additional ISR photons are generated collinear to the e^+ or e^- beams with the structure function method [29]. Additional FSR radiation is implemented at NLO with PHOTOS [30]. As the structure function method relies on a resummation of leading logarithms, it takes into account real and virtual higher-order contributions, although in an approximate way. AFKQED hence provides simulated samples with explicit higher order topologies, such as one additional ISR photon and one additional FSR photon or multiple ISR emission occurring on both beams. In the samples used in this analysis, a minimum mass $m_{X\gamma} > 8$ GeV/c^2 imposed at generation limits the additional ISR energy to 2.3 GeV.

Appendix B: Background normalization. The main backgrounds in the pion channel are $e^+e^- \to q\bar{q}$, dominant at high mass, and $e^+e^- \to \pi^+\pi^-\pi^0\gamma$ dominant at low mass. Their estimates are normalized using the data in the 2D-χ^2 selected region, where they amount to 0.7% and 2.4% of the expected signal, respectively. From the comparison of data and simulated yields of π^0 that mimic an ISR photon, the *uds* background is scaled by a factor 0.422 ± 0.025. For the 3π channel dominated by the production of ω and ϕ resonances, normalization is obtained from reconstructing π^0 from non-ISR photons and comparing the resonance peaks in the $\pi^+\pi^-\pi^0$ spectrum in data and MC samples. A scale factor of 1.013 ± 0.021 is applied to the $3\pi\gamma$ MC. For the other ISR background channels, weights are applied to the MC events depending on the hadronic mass to correct for differences between MC mass distributions and spectra measured at *BABAR*.

Appendix C: Angular resolution of the 0C calculation. Resolution of $\theta_{\gamma_{0C}}$ determination is estimated on MC events by comparing the value calculated from truth information with the value calculated from the reconstructed quantities. As seen in Fig. 3(a), resolution induces a reconstructed/true ratio much larger than unity at low angles, hence opposite to the data/PHOKHARA deficit. The angular resolution is estimated in muon data and MC by comparing the calculated polar angle $\theta_{\gamma_{0C}}$ with the fitted one from the $\gamma_{ISR}\gamma_{LA}$ fit, as shown in Fig. 5 for $E^*_{\gamma_{0C}} > 0.2$ GeV. There is good agreement between data and simulation for the core of the resolution function, with rms values of 30 mrad with little dependence on $\theta_{\gamma_{0C}}$, but tails above 0.5 rad are more important in data. The resulting larger transfer of photons from the dominant sharp radiation peaks along the incident beams towards large angles is estimated to enhance the data/MC ratio by $\sim$10% in the central $\theta_{\gamma_{0C}}$ region, as observed in Fig. 3(a).
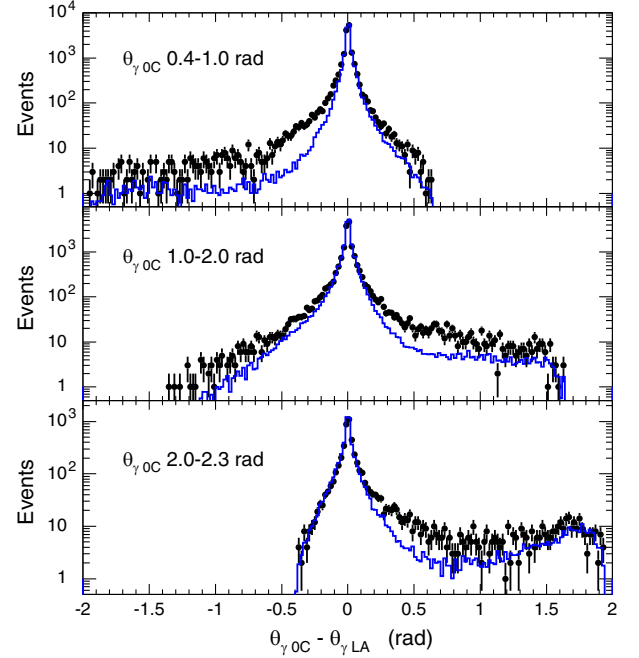

FIG. 5. Distribution of angular differences between the calculated angles $\theta_{\gamma_{0C}}$ and the measured one $\theta_{\gamma_{LA}}$ from the $\gamma_{ISR}\gamma_{LA}$ fit, in three $\theta_{\gamma_{0C}}$ intervals in which the additional photon is within the angular detector acceptance: data points and MC histograms (blue).

Appendix D: FSR and LA-ISR separation. The distribution of the minimum angle $\theta_{\min(trk,\gamma_{LA})}$ between the LA photon and one of the two tracks is shown in Fig. 6 for the $\mu\mu\gamma_{ISR}\gamma_{LA}$ data sample. The two components are fitted using FSR and LA-ISR templates. As LA-ISR is absent in AFKQED, the LA photons are due uniquely to FSR and their $\theta_{\min(trk,\gamma_{LA})}$ distribution provides the FSR template. In PHOKHARA both components are present and the LA-ISR template is obtained by subtracting the FSR template normalized to the yield below 10° from
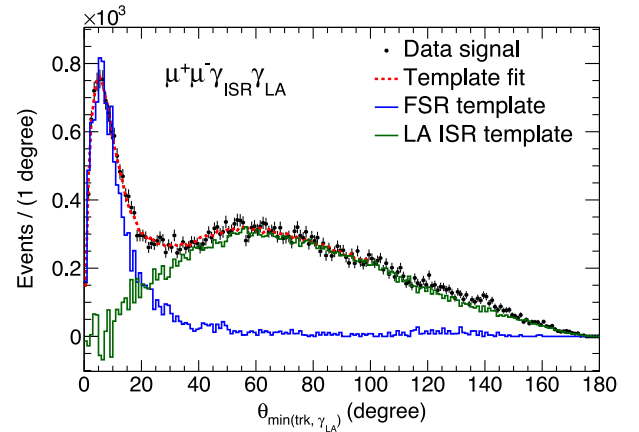

FIG. 6. Template fit separating FSR events from LA ISR events in the $\mu\mu\gamma_{ISR}\gamma_{LA}$ data sample.
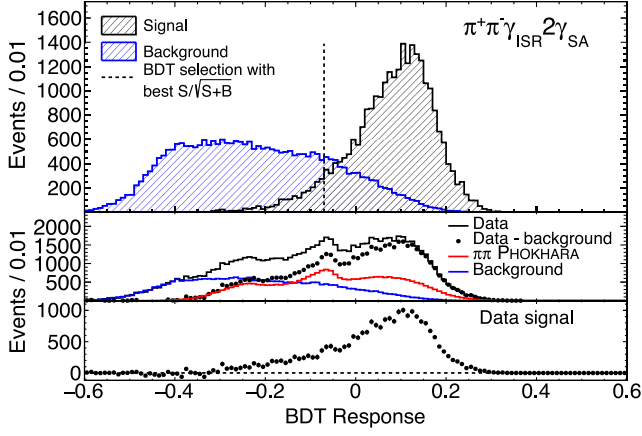
FIG. 7.   BDT response distributions for the training samples (top panel); BDT response distributions showing data and different background components (middle and bottom panels).

the total distribution. The template fit of the data $\theta_{\min(\mathrm{trk},\gamma_{\mathrm{LA}})}$ distribution allows us to measure the relative rates of the two components. Template fits are similarly applied in the $\pi\pi\gamma_{\mathrm{ISR}}\gamma_{\mathrm{LA}}$ sample and to $\theta_{\min(\mathrm{trk},\gamma_{\mathrm{LA}})}$ distributions in $\gamma_{\mathrm{ISR}}\gamma_{\mathrm{SA}}\gamma_{\mathrm{LA}}$ and $\gamma_{\mathrm{ISR}}2\gamma_{\mathrm{LA}}$ samples.

Appendix E: BDT selections. BDT techniques are used at several steps of this analysis: (i) to select clean *uds* and ISR $2\pi\pi^0$ samples to properly normalize these backgrounds; (ii) to optimize the 2D-χ^2 selection; (iii) to reduce backgrounds in NNLO pion samples. As an example, the BDT designed to select the $\gamma_{\mathrm{ISR}}2\gamma_{\mathrm{SA}}$ pion signal uses discriminant variables as the γ_{ISR} energy and angles with respect to other photons and tracks, multiplicity and total energy of additional photons, and the pion angle with respect to the ISR photon direction in the dipion c.m. system. The signal training sample is from the NNLO AFKQED events satisfying the χ^2 and SA photon energy requirements of the $\gamma_{\mathrm{ISR}}2\gamma_{\mathrm{SA}}$ selection, while background is from simulation of non-$\pi\pi$ processes. Figure 7 shows the corresponding BDT response distributions for signal and backgrounds (top) and the comparison between data and backgrounds (bottom). The good agreement of the data and non-$\pi\pi$ background in the far-negative BDT response region indicates that the background estimation is satisfactory. The response of the NLO background taken from PHOKHARA is also well simulated. The selection applied maximizes the signal-over-background ratio and results in a BDT efficiency of 0.926(2) (where the uncertainty is statistical).

Appendix F: The BABAR data-driven approach. Previous and ongoing measurements of the $\pi\pi$ cross
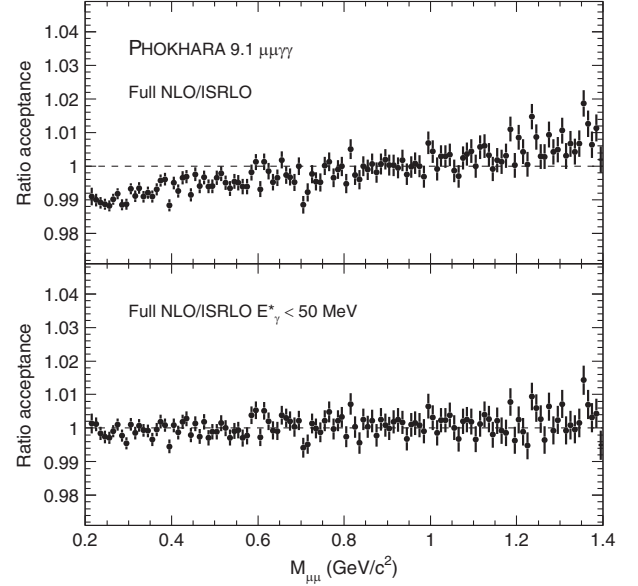

FIG. 8.   Ratio of the *BABAR* acceptance for full NLO to LO acceptance for $\mu\mu\gamma(\gamma)$ PHOKHARA events. Top: full NLO. Bottom: virtual + soft NLO ($E_\gamma^* < 50$ MeV).

section in *BABAR* rely on NLO kinematic fits that explicitly include one photon in addition to γ_{ISR}. Although some higher order events may be rejected by the NLO fits, this loss is corrected for by the 2D-χ^2 efficiency measured on the data [4,5]. It is only when calculating the event acceptance prior to the kinematic fits that generator dependence occurs.

To quantify the effect of the overestimated hard NLO contribution in PHOKHARA, the *BABAR* acceptance is computed as a function of mass at LO and NLO levels using different options of the generator. Figure 8 shows the ratio of NLO/LO acceptances, for full NLO events (top) or events with hard NLO ($E_\gamma^* > 50$ MeV) excluded (bottom). Final states at LO (no generated additional photon) have the same acceptance as virtual + soft NLO events (no hard additional photon) at better than 1 per mil [Fig. 8 (bottom)]. In contrast, hard NLO radiation does affect the acceptance, with a small variation in mass within 1% [Fig. 8 (top)]. This acceptance correction, which needs to be computed from PHOKHARA, is however strongly correlated between the $\pi\pi\gamma(\gamma)$ and $\mu\mu\gamma(\gamma)$ processes, and therefore the effect largely vanishes when taking their ratio for the $\pi\pi$ cross section measurement, for an overall acceptance correction of (0.9981 ± 0.0004), constant with mass from threshold up to 1.4 GeV/c^2. The systematic bias induced by the hard NLO excess observed in PHOKHARA and the missing hard NNLO component is estimated from this result to be $(0.3 \pm 0.1) \times 10^{-3}$.

[1] T. Aoyama *et al.*, Phys. Rep. **887**, 1 (2020).

[2] B. Abi *et al.* (Muon g-2 Collaboration), Phys. Rev. Lett. **126**, 141801 (2021).

[3] D. P. Aguillard *et al.* (Muon g-2 Collaboration), Phys. Rev. Lett. **131**, 161802 (2023).

[4] B. Aubert *et al.* (*BABAR* Collaboration), Phys. Rev. Lett. **103**, 231801 (2009).

[5] J. P. Lees *et al.* (*BABAR* Collaboration), Phys. Rev. D **86**, 032013 (2012).

[6] F. Ambrosino *et al.* (KLOE Collaboration), Phys. Lett. B **670**, 285 (2009).

[7] F. Ambrosino *et al.* (KLOE Collaboration), Phys. Lett. B **700**, 102 (2011).

[8] D. Babusci *et al.* (KLOE Collaboration), Phys. Lett. B **720**, 336 (2013).

[9] A. Anastasi *et al.* (KLOE Collaboration), J. High Energy Phys. 03 (2018) 173.

[10] F. V. Ignatov *et al.* (CMD-3 Collaboration), arXiv:2302 .08834.

[11] S. Borsanyi *et al.*, Nature (London) **593**, 51 (2021).

[12] T. Blum, P. A. Boyle, V. Gülpers, T. Izubuchi, L. Jin, C. Jung, A. Jüttner, C. Lehner, A. Portelli, and J. T. Tsang, Phys. Rev. Lett. **121**, 022003 (2018).

[13] M. Cè *et al.*, Phys. Rev. D **106**, 114502 (2022).

[14] C. Alexandrou *et al.*, Phys. Rev. D **107**, 074506 (2023).

[15] T. Blum *et al.*, Phys. Rev. D **108**, 054507 (2023).

[16] A. Bazavov *et al.*, Phys. Rev. D **107**, 114514 (2023).

[17] J. P. Lees *et al.* (*BABAR* Collaboration), Nucl. Instrum. Methods Phys. Res., Sect. A **726**, 203 (2013).

[18] B. Aubert *et al.* (*BABAR* Collaboration), Nucl. Instrum. Methods Phys. Res., Sect. A **479**, 1 (2002).

[19] B. Aubert *et al.* (*BABAR* Collaboration), Nucl. Instrum. Methods Phys. Res., Sect. A **729**, 615 (2013).

[20] S. Agostinelli *et al.* (GEANT4 Collaboration), Nucl. Instrum. Methods Phys. Res., Sect. A **506**, 250 (2003).

[21] T. Sjöstrand, Comput. Phys. Commun. **82**, 74 (1994).

[22] S. Jadach, B. Ward, and Z. Was, Comput. Phys. Commun. **130**, 260 (2000).

[23] M. Ablikim *et al.* (BESIII Collaboration), Phys. Lett. B **753**, 629 (2016); **812**, 135982(E) (2021).

[24] T. Xiao, S. Dobbs, A. Tomaradze, K. K. Seth, and G. Bonvicini, Phys. Rev. D **97**, 032012 (2018).

[25] T. Kinoshita, J. Math. Phys. (N.Y.) **3**, 650 (1962); T. D. Lee and M. Nauenberg, Phys. Rev. **133**, B1549 (1964).

[26] F. Campanario, H. Czyż, J. Gluza, M. Gunia, T. Riemann, G. Rodrigo, and V. Yundin, J. High Energy Phys. 02 (2014) 114.

[27] H. Czyż and J. H. Kühn, Eur. Phys. J. C **18**, 497 (2001).

[28] S. Binner, J. H. Kühn, and K. Melnikov, Phys. Lett. B **459**, 279 (1999).

[29] M. Caffo, H. Czyż, and E. Remiddi, Nuovo Cimento A **110**, 515 (1997).

[30] E. Barberio, B. van Eijk, and Z. Was, Comput. Phys. Commun. **66**, 115 (1991).